Acoustic radiation from an engine intake using an admittance multimodal method

Bruno Mangin, Majd Daroukh, Gwenael Gabard

Bruno Mangin, Majd Daroukh, Gwenael Gabard. Acoustic radiation from an engine intake using an admittance multimodal method. INTERNOISE 2023, Aug 2023, Tokyo, Japan. hal-04439567

HAL Id: hal-04439567
https://hal.science/hal-04439567v1
Submitted on 5 Feb 2024

Acoustic radiation from an engine intake using an admittance multimodal method

Bruno Mangin[1], Majd Daroukh[2]
DAAA, ONERA
Paris Saclay University F-92322 Châtillon, France

Gwénaël Gabard[3]
Acoustics Laboratory of the University of Le Mans (LAUM)
UMR 6613, Institute of Acoustics - Graduate School (IA-GS), CNRS, Le Mans University, France

ABSTRACT

This paper presents an adaptation of the admittance multimodal method for computing the mean flow around an engine intake and the associated radiated acoustic field. The basic idea is to surround the engine with a fictive duct with a perfectly matched layer on its outer wall which simulates far-field conditions and avoids any acoustic reflection. The use of matching conditions between this duct and the engine duct allows for calculating the flow and acoustic admittance matrices (and then the associated fields) everywhere. The developed method, initially devoted to acoustic propagation, can also compute the mean flow field with some adjustments and is very efficient if some assumptions are added (typically an incompressible flow hypothesis in the far-field). The flow and acoustic results are then compared against a finite element method and highlight the accuracy and efficiency of the proposed approach.

1. INTRODUCTION

The intake of aircraft engines plays a frequency high-pass filter role which leads to an exponential decay of cutoff modes, that can therefore generally be neglected. However, the evolution of engines towards ultra high bypass ratio (UHBR) architectures has come with a shortening of the engine nacelle for weight and drag reasons. This shortening significantly reduces the high-pass filter efficiency of the duct. Therefore, it now becomes essential to account for these cut-off modes in the prediction methods. Analytical models based on the Kirchhoff-Helmholtz method could be used to address their radiation from the engine intake [1, 2, 3]. However, a more complex modelling is needed to accurately predict the directivity patterns [4, 5]. Numerical simulations can be used to overcome these difficulties. Among them, the finite element method (FEM) applied to the potential equation is a powerful tool for computing acoustic far-field radiation but can be computationally expensive. The current paper proposes an alternative and less computationally demanding multimodal approach. This method has already been used for computing the acoustic radiated field and has demonstrated high performance, making it suitable for optimization procedures [6, 7, 8]. However, like most multimodal methods, it is currently limited to cases without mean flow. Previous articles have been devoted to the adaptation

---

[1] bruno.mangin@onera.fr

[2] majd.daroukh@onera.fr

[3] gwenael.gabard@univ-lemans.fr

of the method to flow cases for in-duct computations [9, 10]. In this article, we propose to extend to flow cases the multimodal method with radiation.

The original multimodal method with the radiation problem involves considering an isolated duct surrounded by a fictive one with a larger radius and a perfectly matched annular layer (PML) on its outer wall. This PML simulates an infinite domain by damping the waves that propagate inside. In this article, we present a revised approach that considers in addition the presence of a mean flow. At first, we rewrite the perturbation equation to account for the presence of a mean flow in a duct with PML walls. Then we show that these equations can also be applied to compute the mean flow by modifying the definition of the admittance matrices at the end of the ducts and by carrying out an induction process on the density, as done in [10].

The paper is structured as follows. Section 2 provides a brief overview of the equations governing the flow and acoustic fields and introduces the concept of PML walls. In section 3, we develop the multimodal equations in a duct with PML walls in the presence of heterogeneous potential flow. Section 4 explains the numerical procedure used to validate the method. The developed method is then compared against a FEM code in section 5 where a parametric study is conducted. Finally, section 6 presents the conclusions and discussions of the study.

2. DESCRIPTION OF THE PROBLEM

2.1. Governing equations in a hard-walled duct

When performing acoustic calculations for an aircraft at take-off and approach conditions, the flow properties are typically assumed to be those of an ideal gas with no viscous or thermal effects. These assumptions, combined with an irrotational hypothesis for the flow in the intake, allow us to model the unsteady velocity field of the flow as the gradient of a potential function.

In the following, all the parameters are transformed to be dimensionless (see [11] for more details). The velocity vector, density, speed of sound and potential variables are written $\tilde{\mathbf{v}} = \mathbf{V} + \mathrm{Re}(\mathbf{v}\ \mathrm{e}^{i\omega t}) = (U, V, W) + \mathrm{Re}((u, v, w)\ \mathrm{e}^{i\omega t})$, $\tilde{\rho} = D + \mathrm{Re}(\rho\ \mathrm{e}^{i\omega t})$, $\tilde{c} = C + \mathrm{Re}(c\ \mathrm{e}^{i\omega t})$ and $\tilde{\phi} = \Phi + \mathrm{Re}(\phi\ \mathrm{e}^{i\omega t})$ respectively. Capital letters are linked to the mean flow variables and lower-case letters to the acoustic variables. With these hypotheses and notations, the equations that govern the mean flow are:

$$\nabla \cdot (D\nabla\Phi) = 0, \quad \mathbf{V} = \nabla\Phi, \quad \frac{D^{\gamma-1}}{\gamma - 1} + \frac{1}{2}\nabla\Phi \cdot \nabla\Phi = E, \tag{1}$$

where γ is the ratio of specific heats and E is a Bernoulli constant, and the equation that governs the acoustics writes:

$$\nabla \cdot (D\nabla\phi) - D(i\omega + \mathbf{V} \cdot \nabla)\left[\frac{1}{C^2}(i\omega + \mathbf{V} \cdot \nabla)\phi\right] = 0. \tag{2}$$

Hard-wall boundary conditions are considered at the wall for both the mean flow and the acoustics. They write:

$$\nabla\Phi \cdot \mathbf{n} = 0, \;\; \nabla\phi \cdot \mathbf{n} = 0, \tag{3}$$

with $\mathbf{n}$ the unit outgoing vector normal to the surface.

2.2. Governing equations in a duct with a PML wall

The goal is to simulate the propagation of acoustic waves within an isolated nacelle, without any external support, and then radiate the resulting sound waves in the near field. To achieve this, we model the nacelle as an axisymmetric waveguide and surround it with a duct that has a PML on its outer wall to model far-field radiation conditions. This is illustrated in Figure 1. It appears that the computational domain can be separated into three regions $\mathcal{A}$, $\mathcal{B}$ and $\mathcal{C}$. In the waveguide $\mathcal{A}$, the propagation is a standard in-duct acoustic propagation, while in the regions $\mathcal{B}$ and $\mathcal{C}$, the propagation occurs in a duct with a PML outer wall.

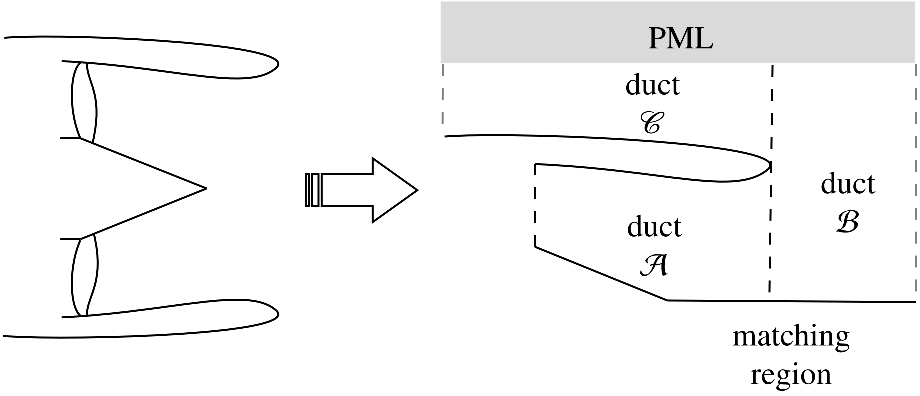

Figure 1: Sketch of a generic turbofan inlet and the associated free-field radiation problem.

The equation governing the acoustic propagation inside an hard-walled duct has been given in the section 1. Now in the scope of simulating far-field boundary conditions, this equation is slightly modified to account for a PML. This PML is defined using the function α which aims to modify the radial coordinate r into a stretched on $\widetilde{r}$ and to damp the acoustic waves. Its values are complex numbers inside the PML and are equal to one elsewhere [12]. Here the function α is chosen to be:

$$\alpha = 1 + 2(\overline{\alpha} - 1)\frac{r - (R_2 - \delta)}{\delta}, \tag{4}$$

with δ the size of the PML, R_2 the radius of the outer duct and $\overline{\alpha}$ a complex number. When this parameter is used, the radial derivative and the radius can be rewritten: $\partial_{\widetilde{r}} = \alpha^{-1}\partial_r$ and $\widetilde{r} = \beta r$, with

$$\beta = 1 + (\overline{\alpha} - 1)\frac{(r - (R_2 - \delta))^2}{\delta}. \tag{5}$$

In such a duct, the equation (2) becomes:

$$\begin{aligned} &\alpha\beta\frac{\partial}{\partial x}\left(D\frac{\partial\phi}{\partial x}\right) + \nabla_\perp \cdot (DH\nabla_\perp\phi) \\ &- D\alpha\beta\left(\mathrm{i}\omega + U\frac{\partial}{\partial x} + \mathbf{V}_\perp \cdot (L\nabla_\perp)\right)\left[\frac{1}{C^2}\left(\mathrm{i}\omega + U\frac{\partial}{\partial x} + \mathbf{V}_\perp \cdot (L\nabla_\perp)\right)\phi\right] = 0, \end{aligned} \tag{6}$$

where $\perp$ refers to the transverse direction and:

$$H = \begin{pmatrix} \beta/\alpha & 0 \\ 0 & \alpha/\beta \end{pmatrix}, L = \begin{pmatrix} \beta & 0 \\ 0 & \alpha \end{pmatrix}. \tag{7}$$

The boundary conditions write:

$$(\frac{\partial\phi}{\partial x}\mathbf{e}_x + L\nabla_\perp\phi) \cdot \mathbf{n} = 0. \tag{8}$$

3. MULTIMODAL EQUATIONS

3.1. Main equation

The in-duct multimodal method derived in [10] can be applied in the duct $\mathscr{A}$. We aim to use the same method in the ducts $\mathscr{B}$ and $\mathscr{C}$, but we do not yet have the multimodal equations in the presence of a PML wall. Therefore, the goal is here to obtain those equations. We begin by writing the weak formulation of the equation (6) over a transverse cross section S bounded by a contour Λ. It writes after some manipulations:

$$\begin{aligned}
&\frac{\mathrm{d}}{\mathrm{d}x}\left(\int_S D\alpha\beta(1-M_x^2)ug^* - \frac{DU}{C^2}\alpha\beta\left(\mathrm{i}\omega + \mathbf{V}_\perp\cdot(L\nabla_\perp)\right)\phi g^*(\mathrm{d}S\right) = \\
&+\int_S\Bigg[D\alpha\beta(1-M_x^2)u\frac{\partial g^*}{\partial x} + DH\nabla_\perp g^*\cdot\nabla_\perp\phi \\
&-\frac{D}{C^2}\alpha\beta((\mathrm{i}\omega+\mathbf{V}_\perp\cdot(L\nabla_\perp))\,\phi\,(-\mathrm{i}\omega+\mathbf{V}_\perp\cdot(L\nabla_\perp))\,g^* + Uu\,(-\mathrm{i}\omega+\mathbf{V}_\perp\cdot(L\nabla_\perp))\,g^* \\
&+U\frac{\partial g^*}{\partial x}\,(\mathrm{i}\omega+\mathbf{V}_\perp\cdot(L\nabla_\perp))\,\phi)\Bigg]\,\mathrm{d}S
\end{aligned} \tag{9}$$

where g is a test function, $*$ denotes the complex conjugate and $M_x = U/C$ is the axial Mach number.

We then project the variable ϕ and its axial derivative $u = \partial_x\phi$ on transverse cross-section functions as in standard multimodal formulations. This basis is denoted $(\varphi_j)_{j\in\mathbb{N}}$, and the variables write $\phi = \sum_j \phi_j(x)\varphi_j(x,r,\theta)$ and $u = \sum_j u_j(x)\varphi_j(x,r,\theta)$ respectively. The test function g in equation (9) is chosen to be the complex conjugate of a basis function φ_i^*, which yields:

$$\begin{aligned}
&\frac{\mathrm{d}}{\mathrm{d}x}\left(\int_S D\alpha\beta(1-M_x^2)\varphi_j\varphi_i^* u_j - \frac{DU}{C^2}\alpha\beta\left(\mathrm{i}\omega+\mathbf{V}_\perp\cdot(L\nabla_\perp)\right)\varphi_j\varphi_i^*\phi_j\mathrm{d}S\right) = \\
&+\int_S\Bigg[D\alpha\beta(1-M_x^2)\varphi_j\frac{\partial\varphi_i^*}{\partial x}u_j + DH\nabla_\perp\varphi_i^*\cdot\nabla_\perp\varphi_j\phi_j \\
&-\frac{D}{C^2}\alpha\beta((\mathrm{i}\omega+\mathbf{V}_\perp\cdot(L\nabla_\perp))\,\varphi_j\,(-\mathrm{i}\omega+\mathbf{V}_\perp\cdot(L\nabla_\perp))\,\varphi_i^*\phi_j \\
&+U\varphi_j\,(-\mathrm{i}\omega+\mathbf{V}_\perp\cdot(L\nabla_\perp))\,\varphi_i^* u_j + U\,(\mathrm{i}\omega+\mathbf{V}_\perp\cdot(L\nabla_\perp))\,\varphi_j\frac{\partial\varphi_i^*}{\partial x}\phi_j)\Bigg]\,\mathrm{d}S.
\end{aligned} \tag{10}$$

This gives the equation that governs the axial variation of the base function amplitudes $(\boldsymbol{\phi},\mathbf{u}) = (\phi_j, u_j)_{j\in\mathbb{N}}$ in a duct with a PML wall:

$$\begin{pmatrix} A_{11} & 0 \\ A_{21} & A_{22}\end{pmatrix}\frac{\mathrm{d}}{\mathrm{d}x}\begin{pmatrix}\boldsymbol{\phi}\\ \mathbf{u}\end{pmatrix} = \begin{pmatrix} M_{11} & M_{12} \\ M_{21} & M_{22}\end{pmatrix}\begin{pmatrix}\boldsymbol{\phi}\\ \mathbf{u}\end{pmatrix}, \tag{11}$$

with:

$$\begin{aligned}
(A_{11})_{ij} &= (M_{12})_{ij} = \int_S D\alpha\beta(1-M_x^2)\varphi_j\varphi_i^*\mathrm{d}S, \\
(M_{11})_{ij} &= -\int_S D\alpha\beta(1-M_x^2)\frac{\partial\varphi_j}{\partial x}\varphi_i^*\mathrm{d}S, \\
(A_{21})_{ij} &= -\int_S \frac{DU}{C^2}\alpha\beta\left(\mathrm{i}\omega+\mathbf{V}_\perp\cdot(L\nabla_\perp)\right)\varphi_j\varphi_i^*\mathrm{d}S, \\
(A_{22})_{ij} &= \int_S D\alpha\beta(1-M_x^2)\varphi_j\varphi_i^*\mathrm{d}S, \\
(M_{21})_{ij} &= \frac{\mathrm{d}}{\mathrm{d}x}\left(\int_S \frac{DU}{C^2}\alpha\beta\left(\mathrm{i}\omega+\mathbf{V}_\perp\cdot(L\nabla_\perp)\right)\varphi_j\varphi_i^*\mathrm{d}S\right) + \int_S DH\nabla_\perp\varphi_i^*\cdot\nabla_\perp\varphi_j\mathrm{d}S \\
&\quad-\int_S\frac{D}{C^2}\alpha\beta\left((\mathrm{i}\omega+\mathbf{V}_\perp\cdot(L\nabla_\perp))\,\varphi_j\,(-\mathrm{i}\omega+\mathbf{V}_\perp\cdot(L\nabla_\perp))\,\varphi_i^* + U\,(\mathrm{i}\omega+\mathbf{V}_\perp\cdot(L\nabla_\perp))\,\varphi_j\frac{\partial\varphi_i^*}{\partial x}\right)\mathrm{d}S, \\
(M_{22})_{ij} &= -\frac{\mathrm{d}}{\mathrm{d}x}\left(\int_S D\alpha\beta(1-M_x^2)\varphi_j\varphi_i^*\mathrm{d}S\right) \\
&\quad+\int_S D\alpha\beta(1-M_x^2)\varphi_j\frac{\partial\varphi_i^*}{\partial x}\mathrm{d}S - \int_S\frac{DU}{C^2}\alpha\beta\varphi_j\left(-\mathrm{i}\omega+\mathbf{V}_\perp\cdot(L\nabla_\perp)\right)\varphi_i^*\mathrm{d}S.
\end{aligned}$$

This is the main equation of the problem that is solved in the ducts $\mathcal{B}$ and $\mathcal{C}$ using the multimodal method. However, the question that remains is how the information is exchanged between the three ducts.

3.2. Matching procedure

At the junction between the ducts, it is necessary to have a formulation that links the admittance matrix Y (defined such that $\mathbf{u} = Y\boldsymbol{\phi}$) of each duct and another one that relates the potential amplitudes $\boldsymbol{\phi}$. We impose continuity on the potential and use the mass conservation equation to obtain these conditions. At the interfaces between the ducts, this implies that [6]:

$$\begin{aligned} \int_{\mathcal{A}} \left(\varphi_i^{\mathcal{A}}\right)^* \phi_{\mathcal{A}}\,\mathrm{d}S &= \int_{\mathcal{A}} \left(\varphi_i^{\mathcal{A}}\right)^* \phi_{\mathcal{B}}\,\mathrm{d}S, \\ \int_{\mathcal{C}} \left(\varphi_i^{\mathcal{C}}\right)^* \phi_{\mathcal{C}}\,\mathrm{d}S &= \int_{\mathcal{C}} \left(\varphi_i^{\mathcal{C}}\right)^* \phi_{\mathcal{B}}\,\mathrm{d}S, \\ \int_{\mathcal{B}} \left(\varphi_i^{\mathcal{B}}\right)^* D u_{\mathcal{B}}\,\mathrm{d}S &= \int_{\mathcal{A}} \left(\varphi_i^{\mathcal{B}}\right)^* D u_{\mathcal{A}}\,\mathrm{d}S + \int_{\mathcal{C}} \left(\varphi_i^{\mathcal{B}}\right)^* D u_{\mathcal{C}}\,\mathrm{d}S, \end{aligned} \tag{12}$$

where the subscripts and exponents $\mathcal{A}$, $\mathcal{B}$, and $\mathcal{C}$ indicate that the variables or integrals are associated with the ducts $\mathcal{A}$, $\mathcal{B}$, and $\mathcal{C}$ respectively. In a matrix form, this writes:

$$\begin{gathered} \boldsymbol{\phi}_{\mathcal{A}} = F^{\mathcal{B}}_{\mathcal{A}} \boldsymbol{\phi}_{\mathcal{B}}, \quad \boldsymbol{\phi}_{\mathcal{C}} = G^{\mathcal{B}}_{\mathcal{C}} \boldsymbol{\phi}_{\mathcal{B}}, \\ \mathbf{u}_{\mathcal{B}} = F^{\mathcal{A}}_{\mathcal{B}} \mathbf{u}_{\mathcal{A}} + G^{\mathcal{C}}_{\mathcal{B}} \mathbf{u}_{\mathcal{C}}, \end{gathered} \tag{13}$$

where $(F^{\mathcal{B}}_{\mathcal{A}})_{ij} = \int_{\mathcal{A}} (\varphi_i^{\mathcal{A}})^* \varphi_j^{\mathcal{B}} w_{\mathcal{A}} \mathrm{d}S$ is the transfer matrix from duct $\mathcal{B}$ to duct $\mathcal{A}$, $(G^{\mathcal{B}}_{\mathcal{C}})_{ij} = \int_{\mathcal{C}} (\varphi_i^{\mathcal{C}})^* \varphi_j^{\mathcal{B}} w_{\mathcal{C}} \mathrm{d}S$ is the transfer matrix from duct $\mathcal{B}$ to duct $\mathcal{C}$, and $\varphi_i^{\mathcal{A}}, \varphi_i^{\mathcal{C}}$ are orthogonal with respect to the weights functions $w_{\mathcal{A}}, w_{\mathcal{C}}$ respectively. The admittance at the exit of the duct $\mathcal{A}$ is therefore:

$$Y_{\mathcal{A}} = (F^{\mathcal{B}}_{\mathcal{A}} Y_{\mathcal{B}}^{-1} (I_d + G^{\mathcal{B}}_{\mathcal{C}} Y_{\mathcal{C}} G^{\mathcal{C}}_{\mathcal{B}})^{-1} F^{\mathcal{A}}_{\mathcal{B}})^{-1}. \tag{14}$$

The admittances $Y_{\mathcal{B}}$ and $Y_{\mathcal{C}}$ are found by applying a multimodal method inside the ducts $\mathcal{B}$ and $\mathcal{C}$ from their initial value at far-field to the matching region.

3.3. Mean flow computation

In a previous paper [10], it was shown that the multimodal approach could also be used to compute the mean flow. The basic idea is that the equation that governs the acoustic propagation without base flow and at zero frequency is equivalent to the one that governs the mean flow provided that the density is known. Therefore, a mean flow computation can be performed using an acoustic approach. To obtain the mean flow density, a convergence process is applied. However, the acoustic computation becomes unstable when performed at zero frequency with a complex PML. Therefore, for the flow computations, the PML is turned off and a large outer radius is chosen for the surrounding duct so that the flow at its outer wall approximately matches the free-field desired Mach number.

Enforcing the ratio between the potential and axial velocity amplitudes associated with the "plane wave" is another issue to consider when dealing with flow computations. For a single duct, this is not a problem as the potential is defined up to a constant. Thus, imposing this ratio only fixes the potential constant and has no impact on the results. However, in cases where multiple ducts are present, it becomes necessary to enforce this ratio at different axial locations. It must be done in the ducts $\mathcal{B}$ and $\mathcal{C}$ in our case (in order to find $Y_{\mathcal{B}}$ and $Y_{\mathcal{C}}$ at the junction location). While one of the two values can still be freely imposed to fix the potential constant, the other enforces a specific mass flow distribution between the three ducts. We then conduct a convergence process to determine the value of this second potential-to-velocity ratio required to ensure the desired mass flow distribution. One could use a random guess for the initial value, but this would be time-consuming. A good guess for this initial value can be obtained easily because the flow should be constant near the outer wall of the upper duct since we want to represent free-field conditions. Indeed, in the free field, the potential can be written $\Phi_\infty = U_\infty x + cst$ where U_∞ is the free-stream axial velocity (defined by the user). If the constant is fixed by choosing an arbitrary potential-to-velocity ratio in duct $\mathscr{B}$, then the initial guess of the potential-to-velocity ratio in duct $\mathscr{C}$ can be determined. Finally, the convergence process on this second ratio stops when the Mach at the end of duct $\mathscr{C}$ equals M_∞.

4. VALIDATION PROCEDURE

4.1. Computation hypotheses

The computation can be directly carried out using the formulation derived in the previous section. However, this does not offer any significant advantage compared to finite element methods. In particular, the flow computation would be time-consuming due to the need for many polynomials in the duct $\mathscr{B}$ to represent the strong velocity gradient near the stagnation point that appears near the nacelle lip. Therefore, the flow is assumed to be incompressible in the duct $\mathscr{B}$ which leads to a single point admittance calculation for computing the flow (constant cross-section and no density variation). With this hypothesis, the time taken for the flow computation is similar to the one of an in-duct computation.

4.2. Definition of test cases

A geometry representative of a CFM56 engine has been used in the following. The geometry can be found on the GitHub of one of the authors (https://github.com/brumann/CFM56-geometry). The nacelle is placed inside a mean flow with a free-stream Mach number of $M_\infty = 0.2$ and density $D_\infty = 1$, while at the fan plane, the Mach number is $M_f = 0.5$. The tip radius of the outer duct is equal to 3 m. For all cases studied below, the acoustic injected mode is defined such that the root mean square (RMS) pressure at the injection equals one at the outer wall.

4.3. Validation methodology

The validation is done using a FEM [13] which computes both the steady potential flow and the acoustic field. It is important to note that for the FEM, the fan plane is moved backwards since this method requires the flow to be uniform at its boundary, unlike the multimodal method. A mesh convergence process was carried out for all presented test cases for the FEM.

In the case of the multimodal method, as the problem is axisymmetric, a single Fourier mode in the circumferential direction is used. Chebyshev functions are used in the radial direction (this basis is the same as in [9]). In the axial direction, an axial mesh density [8] equal to 0.5 in the ducts $\mathscr{A}$ and $\mathscr{C}$ is used, and 100 points are used in the duct $\mathscr{B}$ (where the mesh criterion can be relaxed because there are minor flow changes and no wall variation). The numerical parameters used in all ducts for the mean flow and acoustic computations are summed up in Table 1.

	Duct $\mathscr{A}$	**Duct $\mathscr{B}$**	**Duct $\mathscr{C}$**	**PML definition**
Mean flow	25 polynomials	200 polynomials	25 polynomials	—
Acoustics	50 polynomials	150 polynomials	100 polynomials	$\delta = 0.5,\ \overline{\alpha} = \exp(i\pi/4)$

Table 1: Summary of the multimodal computation parameters.

5. RESULTS

5.1. Flow results

Three flow computations are conducted, including one with the FEM code and two with the MM code. The first MM computation is performed without assuming an incompressible flow inside the duct $\mathcal{B}$ to demonstrate the method's ability to compute the precise mean flow. The second one is done with the simplification hypothesis to check its validity. Figure 2 displays the axial velocity contours obtained from these three computations. Although there are some minor differences in the region associated with the domain $\mathcal{B}$, the results are generally similar.

The small discrepancies between the FEM and exact MM computation can be attributed to different definitions of the boundary conditions. In fact in the multimodal method, we assume an hardwalled boundary condition at the outer wall while in the FEM the velocity value is fixed. The differences between the full and simplified MM computations, only visible in duct $\mathcal{B}$, are minor and are not expected to affect acoustic computations. Therefore, we only use the flow field resulting from the simplified MM computation in the following.

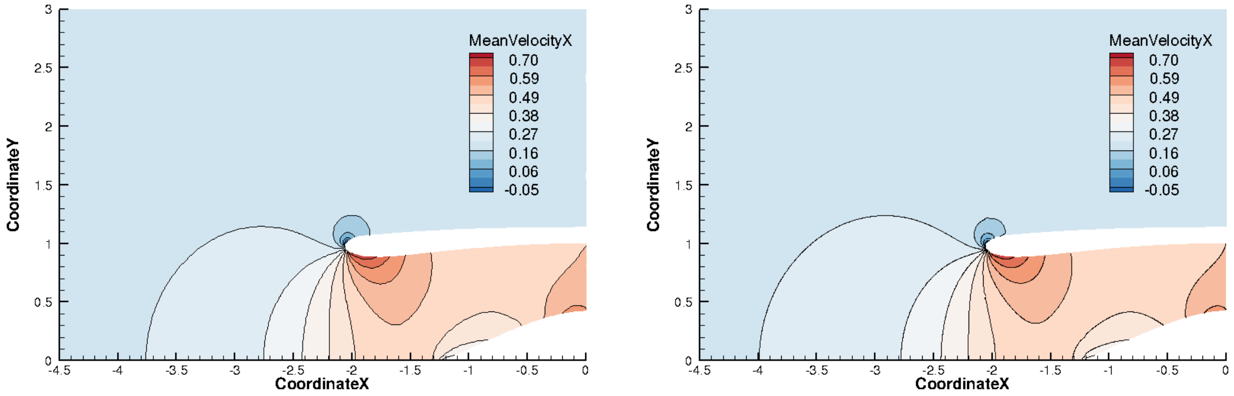

(a) FEM

(b) MM

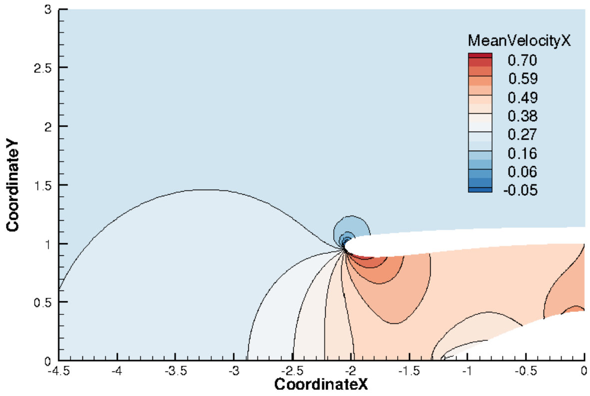

(c) MM with simplifed flow

Figure 2: Contours of normalized axial velocity.

5.2. Qualitative acoustic results

Some qualitative acoustic results are given to assess the multimodal method's capability with a PML wall to represent the radiation condition in the presence of mean flow. The simplified flow is interpolated onto the acoustic grid for multimodal computations. For the FEM simulations which serve as a reference, the same grid is used for the flow and acoustics to avoid errors from grid interpolation.

Figures 3 and 4 depict the sound pressure level (SPL) in dB for the injected modes (m, n) =

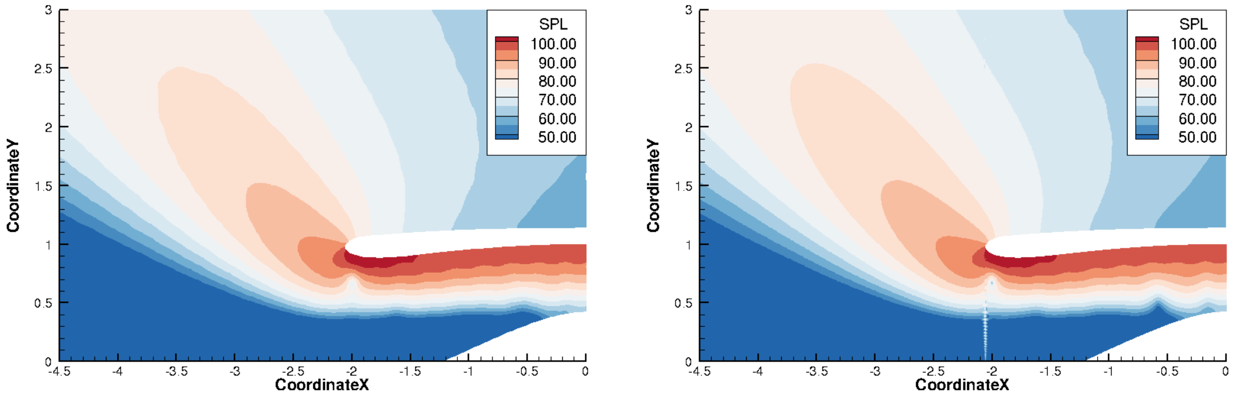

(a) FEM (b) MM

Figure 3: SPL pressure field for a mode $(m, n) = (10, 1)$ at $\omega = 15$.

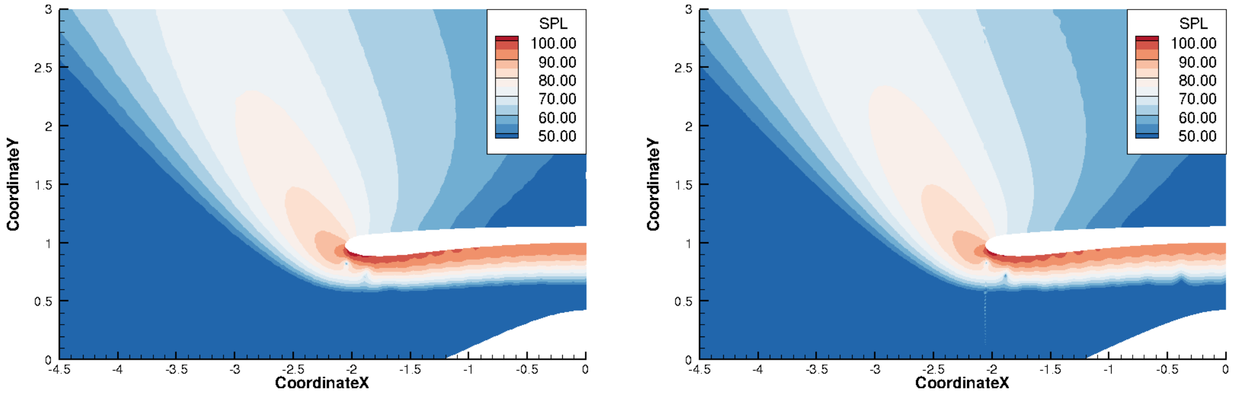

(a) FEM (b) MM

Figure 4: SPL pressure field for a mode $(m, n) = (25, 1)$ at $\omega = 30$.

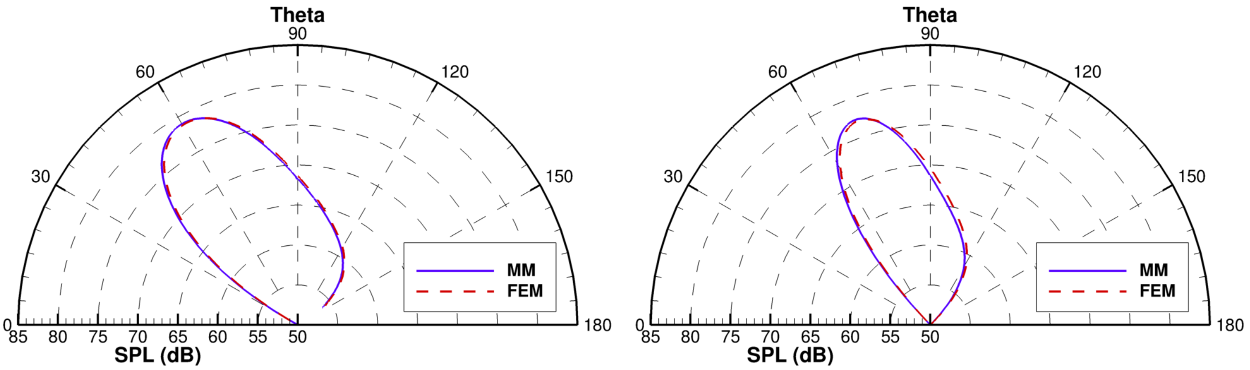

(a) $(m, n) = (10, 1)$ at $\omega = 15$ (b) $(m, n) = (25, 1)$ at $\omega = 30$

Figure 5: SPL directivity for the modes $(m, n) = (10, 1)$ at $\omega = 15$ and $(m, n) = (25, 1)$ at $\omega = 30$.

$(10, 1)$ at $\omega = 15$ and $(m, n) = (25, 1)$ at $\omega = 30$, obtained using the MM and FEM. The two methods yield similar results. However, slight discrepancies can be observed near the injection and are attributed to the differences in the definition of injection conditions. In Figure 3, non-physical perturbations can be seen at the junction level ($x = -2.05$). These perturbations arise due to the appearance of high-order modes generated by the poorly conditioned junction matrices. However, these parasite fluctuations are quickly attenuated and seem not to propagate.

Figure 5 shows the SPL directivity for the two previously studied test cases. The directivity is computed on an arc located 2 m from the engine exit, with 0 degrees corresponding to the forward direction. We use the term "quiet zone" to refer to the area near the engine axis where the SPL is low (below 50 dB). Despite the flow hypothesis used in the MM and the differences in the injection boundary conditions, the radiation pattern given by the method is accurate for both modes, which validates the chosen approach. Note that, as expected for modes close to the transition, the radiation pattern presents one main lobe directed towards the forward arc with a large angle of the quiet zone (peak radiation near 60° and 70°). Investigating if the method also performs well when different acoustic parameters vary is now necessary.

5.3. Parameter study for cut-on modes

In this section, we study the evolution of the directivity with regards to multiple parameters for injected modes which remain cut-on throughout the whole duct. The parameter study encompasses the variation of the nondimensionalized pulsation ω, the circumferential mode order m, and the radial mode order n. FEM computations are also performed to validate the results.

Frequency evolution

The same mode orders as studied above, $(m, n) = (10, 1)$ and $(m, n) = (25, 1)$, are taken but the frequency is multiplied by 1.5 and 2 to evaluate the effects of frequency variation on the radiation pattern. The results are shown in Figure 6. Both methods produce consistent results. Note that the agreement is good for the azimuthal mode $m = 10$ at all frequency but some minor differences are observed for the mode $m = 25$ at high frequency. From a physical perspective, we observe that, the directivity patterns maintain roughly the same peak SPL levels as the pulsation ω increases. But, at low frequencies, the directivity pattern is typically dominated by a single lobe, whereas at higher frequencies, additional lobes appear. This suggests that different radial modes contribute to the radiated field. This phenomenon can be explained by the creation of scattered radial modes within the duct that become cut-on for higher frequencies and thus contribute to the radiated field. Furthermore, we observe that the main radiation lobe is directed towards the forward-arc, which is an expected behaviour given that all modes are cut-on modes. It should also be noted that the size of the quiet zone decreases as the frequency increases, and the angle of the main lobe moves towards the engine axis.

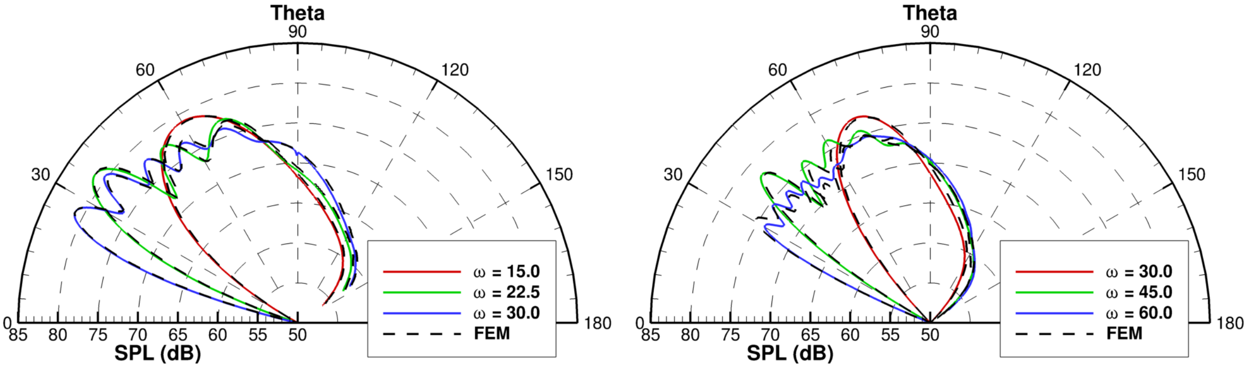

(a) $(m, n) = (10, 1)$

(b) $(m, n) = (25, 1)$

Figure 6: SPL directivity evolution with the increase of the frequency.

Radial order evolution

We start with both modes studied in the qualitative comparison and increase the radial order of the injected mode to check its effect on the directivity. For the frequency, a frequency where all the modes are cut-on is kept. We chose $\omega = 30$ for the azimuthal order $m = 10$ and $\omega = 45$ for the azimuthal order $m = 25$ and look at the first three radial orders. The results are shown in Figure 7. The results obtained using the proposed method are in good agreement with those obtained using the FEM for all radial orders. The first observation is a decrease in the number of lobes in the radiation pattern as the radial order increases. This result may initially seem counter-intuitive, but it can be explained by considering the distance to the transition phenomenon. For instance, for the azimuthal order $m = 10$, when the radial order is $n = 3$, the mode is weakly cut-on, which results in a weak modal scattering [14]. As a result, we observe only three lobes in the directivity pattern. On the other hand, when the radial order is $n = 1$, the mode is well cut-on, and there is significant modal scattering inside the duct, which leads to the five observed main lobes. In addition, we note that the pressure levels are higher in the rear-arc for low radial orders. This behaviour can be attributed to the same reason. Indeed the high-radial order modes generated by scattering mechanisms are weakly cut-on or cut-off, and therefore they tend to have higher levels in the rear-arc [5]. Note that here the size of the quiet zone does not vary for the different radial orders.

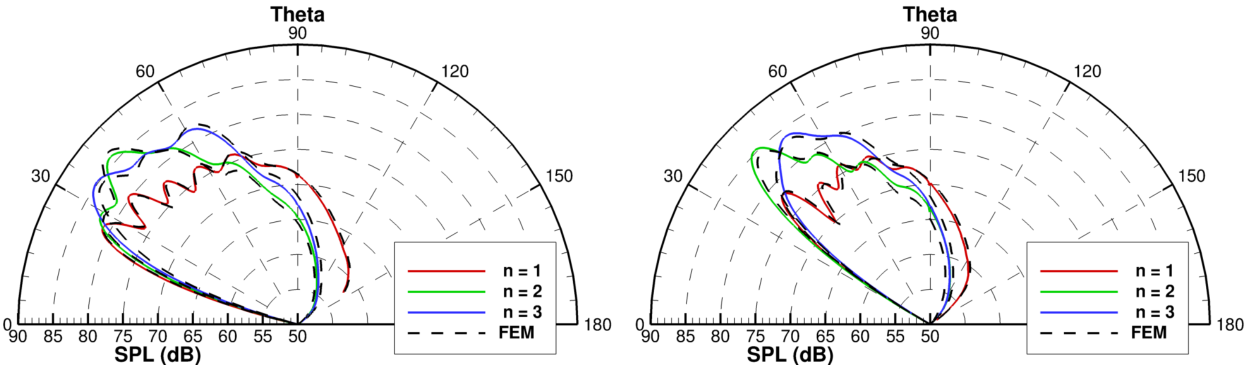

(a) $m = 10$ at $\omega = 30$ (b) $m = 25$ at $\omega = 45$

Figure 7: SPL directivity evolution with the increase of the radial order.

Azimuthal order evolution

Here the impact of the azimuthal order on the directivity pattern is evaluated. The radial order is kept constant and equals one. Three azimuthal orders are considered, $m = 10, 20, 30$ for the pulsation $\omega = 40$. The results are shown in Figure 8. Once again the two methods agree on the directivity patterns. As the azimuthal wavenumber increases, the number of lobes in the radiation pattern decreases. These observations can again be explained by the distance to a transition phenomenon. The further away from it, the more lobes are present in the radiation pattern and the smaller is the angle of the quiet zone. Moreover as the azimuthal wavenumber order increases, the angle of the main lobe increases. Therefore, the effect of the azimuthal mode is at the opposite of the one of the frequency.

5.4. Parameter study for cut-off modes

Since the injection is moved backward in the FEM computation, cut-off comparisons cannot be made as such. Therefore, the source amplitude is increased for the FEM computations to mitigate the exponential decay in this extended part. Both radial order and frequency evolutions are examined to understand their impact on the directivity when the injected mode is cut-off. The radial test cases are conducted at $\omega = 30$ for the azimuthal order $m = 10$, and the frequency test cases are conducted for a mode $(m, n) = (25, 1)$. First, for the azimuthal order $m = 10$, the studied radial order ranges from $n = 6$ to $n = 8$. $n = 6$ is cut-on while the other ones are cut-off. Then, for the azimuthal order $m = 25$, three different frequencies are tested: $\omega = 24.5$, 24.7 and 25. For these frequencies, the source amplitude is multiplied by 10^5 to avoid low SPL in the radiation pattern. The results are plotted

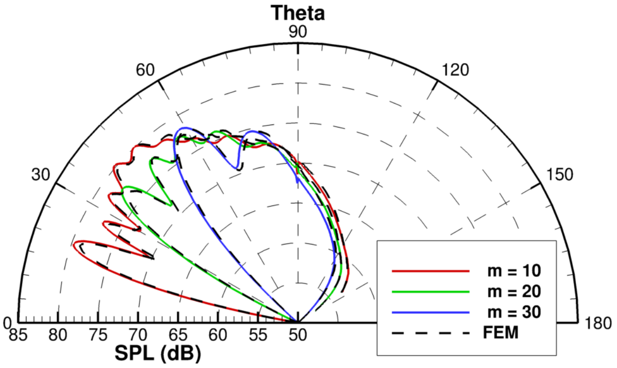

Figure 8: SPL directivity evolution with the increase of the azimuthal order for $n = 1$ at $\omega = 40$.

in Figure 9. Both methods agree on the directivity pattern for all cases except for the challenging mode $(m, n) = (10, 8)$ where we are close to the numerical precision. For the radial order evolution, apart from the exponential decay, scattering phenomena cause the injected mode to have almost no impact. The directivity pattern for modes $n = 7$ and $n = 8$ is close to that of mode $n = 6$. This suggests that the directivity of cut-off modes is not explicitly dependent on the radial order of the injected mode but rather depends on the one of the closest cut-on mode. Note that this conclusion can be derived analytically for a constant cross-section duct by using the far-field directivity formulation derived by Gabard & Astley [15]. The impact of the frequency is not as clear, but it seems that as it increases, the main directivity lobe shifts towards the engine axis. Only one lobe is observed in all cases, which comes from the fact that the injected mode radial order is $n = 1$ and that no cut-on mode that could alter the directivity pattern can be excited.

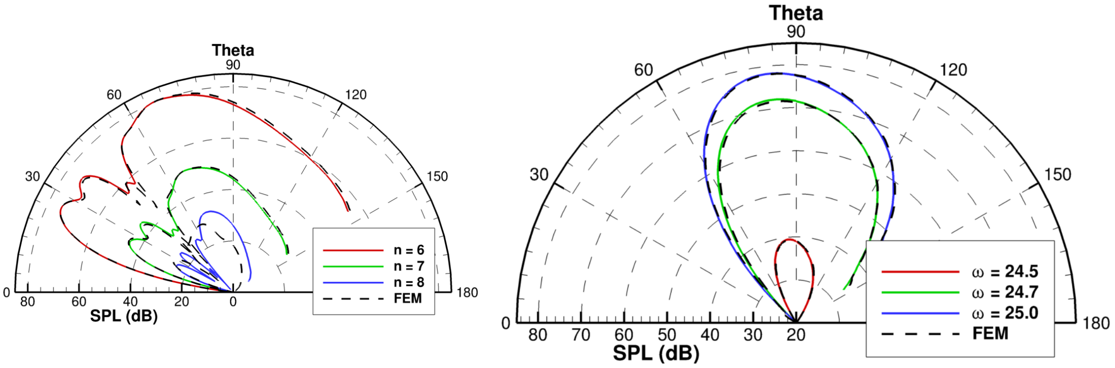

(a) Radial order evolution for $m = 10$ at $\omega = 30$

(b) Frequency evolution for $(m, n) = (25, 1)$

Figure 9: SPL directivity of cut-off modes.

6. CONCLUSIONS

We have developed a modified multimodal method to compute the mean flow around an engine intake and the acoustic radiation from this intake. This was achieved by surrounding the engine with a duct with a perfectly matched layer wall, rewriting the acoustic propagation equation inside this duct, and using connection formulas between the inner and outer ducts. Our proposed approach enables the efficient calculation of the radiated field. The flow computation takes approximately 20 seconds for the presented test cases, while the acoustic computations take between 20 and 60 seconds. Although our method is faster than the FEM for all the presented test cases, the advantage of the method when compared to FEM is not as important as for in-duct computations. Still, the formulation was validated against FEM results and proved to be accurate in computing the mean flow and acoustic fields. A parametric study has also been conducted using this method to understand the impact of various parameters on acoustic radiation. It is found that the distance to the transition drives the main lobe direction, while the highest radial cut-on mode order determines the number of lobes in the radiation pattern.

ACKNOWLEDGMENTS

ONERA carried out these activities in the framework of the ADEC project. This project has received funding from the Clean Sky 2 Joint Undertaking within the European Union's Horizon 2020 research and innovation program, under grant agreement GA ID No. 945583 - LPA IADP 2020-2021.

REFERENCES

1. W. E. Zorumski. Generalized radiation impedances and reflection coefficients of circular and annular ducts. *The Journal of the Acoustical Society of America*, 54(6):1667–1673, 1973.
2. E. J. Rice, M. F. Heidrnann, and T. C. Sofrin. Modal Propagation Angles in a Cylindrical Duct with Flow and their Relation to Sound Radiation. In *17th Aerospace Sciences Meeting*, 1979.
3. S. Lewy. Computation of Broadband Noise Radiated by a Ducted Fan in a Uniform Flow. *International Journal of Acoustics and Vibration*, 8(4):211–218, 2003.
4. S. Guérin. Farfield Radiation of Induct-Cutoff Pressure Waves. In *23rd AIAA/CEAS Aeroacoustics Conference*, 2017.
5. B. Baddour, P. Joseph, A. McAlpine, and R. Leung. Acoustic radiation characteristics of cutoff modes from ducts. *Journal of Sound and Vibration*, 541:117306, 2022.
6. S. Félix, J. B. Doc, and M. Boucher. Modeling of the multimodal radiation from an open-ended waveguide. *The Journal of the Acoustical Society of America*, 143(6):3520–3528, 2018.
7. H. Dong, H. Gao, X. Feng, and Y. Shen. Shape optimization of acoustic horns for improved directivity control and radiation efficiency based on the multimodal method. *The Journal of the Acoustical Society of America*, 149(3):1411–1424, 2021.
8. T. Guennoc. *Modélisation du rayonnement des guides de forme complexe par une méthode multimodale*. PhD thesis, Le Mans université, 2021.
9. B. Mangin, M. Daroukh, and G. Gabard. Propagation of Acoustic Waves in Ducts with Flow Using the Multimodal Formulation. Articles in Advance. *AIAA Journal*, 2023.
10. B. Mangin, M. Daroukh, and G. Gabard. In-duct acoustic and flow computation using the admittance multimodal formulation. Submitted paper. *The Journal of the Acoustical Society of America*, 2023.
11. S. W. Rienstra. Sound transmission in slowly varying circular and annular lined ducts with flow. *Journal of Fluid Mechanics*, 380:279–296, 1999.
12. J. P. Berenger. A perfectly matched layer for the absorption of electromagnetic waves. *Journal of Computational Physics*, 114(2):185–200, 1994.
13. Gwenael Gabard. PFE Software, https://github.com/GwenaelGabard/pfe, 2021.
14. S. W. Rienstra and W. Eversman. A numerical comparison between multiple-scales and finite-element solution for sound propagation in lined flow ducts. *Journal of Fluid Mechanics*, 437:367–384, 2001.
15. G. Gabard and R. J. Astley. Theoretical model for sound radiation from annular jet pipes: far- and near-field solutions. *Journal of Fluid Mechanics*, 549:315–341, 2006.